Applied Surface Science 360 (2016) 98–106

Contents lists available at ScienceDirect

Applied Surface Science

journal homepage: www.elsevier.com/locate/apsusc

A ToF-SIMS investigation of the corrosion behavior of Mg alloy AM50 in atmospheric environments

M. Esmaily*, P. Malmberg, M. Shahabi-Navid, J.E. Svensson, L.G. Johansson

Department of Chemistry and Chemical Engineering, Chalmers University of Technology, SE-412 96 Gothenburg, Sweden

ARTICLE INFO

Article history:
Received 15 October 2015
Accepted 1 November 2015
Available online 4 November 2015

Keywords:
Tof-SIMS
Magnesium alloy
Atmospheric corrosion
Electrolyte
Sub-zero temperature

ABSTRACT

The redistribution of chloride and sodium ions after the NaCl-induced atmospheric corrosion of Mg alloy AM50 was investigated by means of Time-of-Flight Ion Mass Spectroscopy (ToF-SIMS). The samples were exposed at −4 and 22 °C in the presence of 400 ppm CO_2. The results confirm the presence of less conductive electrolyte, and thus, less movement of ionic species (including sodium and chloride) in the electrolyte layer formed on the surface of samples exposed at the sub-zero temperature. Besides, ToF-SIMS analysis showed the presence of an Al-containing surface film formed on the alloy surface after exposure at high relative humidity.

1. Introduction

The high spatial resolution and surface sensitivity of the time-of-flight secondary ion mass spectroscopy (ToF-SIMS) [1,2] implies that the technique is as a powerful tool for analyzing the chemical composition of corroded surfaces. This is especially the case for the analyses where the commonly used techniques such as the energy-dispersive X-ray (EDX) are either restricted in their sensitivity for some elements or have distinctly inferior spatial and/or depth resolution. Still, there are few applications on the use of the ToF-SIMS in corrosion studies of light alloys [3–7], some the major ones are given here. Seyeux et al. [5] studied the film formed on Al_3Mg_2 in water by ToF-SIMS and reported that the film was a mixture of the hydroxides and oxides of Mg and Al. They also reported the presence of MgH_2 in the surface film formed on pure magnesium (Mg) after immersion in water. More recently, Unocic et al. [6] employed ToF-SIMS depth profiling to examine the presence of H species in the films formed on the surface of Mg alloys after some hours of exposures in ^{18}O water and in D_2O. Despite of these studies, the potentials of ToF-SIMS in understanding the corrosion behavior of metallic materials is an area that has been much less researched as compared to other surface sensitive techniques such as X-ray photoelectron spectroscopy (XPS) and auger electron spectroscopy (AES).

In the present paper, which a continuation of a recent study [8], Mg alloy AM50 is subjected to atmospheric corrosion at a constant relative humidity of 95% in the presence of NaCl at −4 and 22 °C. Sub-zero temperature was used as, for *e.g.*, in automotive applications components are subjected to atmospheric corrosion in the presence of NaCl (de-icing salts) in the winter, when temperatures are close to or below 0 °C. Hence, it becomes important to study the atmospheric corrosion behavior of Mg alloys in the presence of NaCl, at low temperatures. As the experiments do not simulate rain, all corrosion products, together with the sodium chloride added before exposure, remain on the corroded surface. Hence, an investigation of the chemical composition of the corroded surface can provide valuable information about the corrosion process. Especially, the presence of anodic and cathodic areas is expected to result in a redistribution of ionic species, especially sodium and chloride ions that can be detected using ToF SIMS. The distribution of *e.g.*, chloride and sodium ions on the corroded surface can also be investigated by means of EDX analysis on plan view SEM images or on the FIB-prepared cross sections. However, the process of producing FIB-prepared cross sections is rather time-consuming and requires several runs in order to find the right position of the pits beneath the corrosion crusts, as the pits are not necessarily located at the center of the corrosion products.

We investigated the distribution of ionic species by ToF-SIMS analysis on samples subjected to atmospheric corrosion in the presence of NaCl at different temperatures. Thus, the objective of the present study was twofold; (a) assessing the usefulness of ToF-SIMS to visualize (3-dimensional rendering) the chemical composition (lateral and depth distribution) of corroded surfaces,

* Corresponding author at: Department of Chemistry and Chemical Engineering, Chalmers University of Technology, SE-412 96 Gothenburg, Sweden.
E-mail address: mohsen.esmaily@chalmers.se (M. Esmaily).

http://dx.doi.org/10.1016/j.apsusc.2015.11.002

Table 1
Composition of the test material (% by weight).

	Al	Zn	Mn	Si	Fe	Cu	Ni	Ca
AM50	5.0	0.01	0.25	0.01	0.0016	0.0010	0.0007	n.a.

and (b) shed light on the corrosion mechanisms occurring at sub-zero temperatures. The ToF SIMS measurements are complemented by determination of mass gain and corrosion rate, and the results provided by some other analytical techniques. The temperature dependence of the atmospheric corrosion of alloy AM50 is addressed.

2. Experimental procedure

Chemical composition of the tested Mg alloy AM50 is listed in Table 1. As-received material was machined to obtain $14 \times 14 \times 3\,mm^3$ corrosion coupons with an exposed surface area of $5.56\,cm^2$ from high pressure die cast (HPDC) AM50 alloy. The test alloy had a typical solidification microstructure of Mg alloys (see [9,10]) consisting of primary α-Mg grains and inter-dendritic regions. Intermetallic β phase particles ($Mg_{17}Al_{12}$) were present in latter regions. Also, because of the presence of about 0.5% (mass) Mn, η phase particles (Al_8Mn_5 (Fe)) were also formed almost everywhere in the microstructure.

Sample preparation procedure, including mechanical grinding and polishing is described elsewhere [8]. A solution of 20 ml distilled water, 80 ml ethanol and 1 g NaCl was sprayed on the test coupons. The samples were contaminated with two different amounts of salt, 14 and 70 μg/cm^2. The experimental set-ups for the exposures at different temperatures have been described in detail previously [8]. Relative humidity (RH) was regulated at 95 ± 0.3%. Carbon dioxide (CO_2) was added from a cylinder to obtain a constant concentration of 400 ± 20 ppm. To monitor the atmospheric corrosion process, at the conclusion of an exposure, after measuring the wet mass, the samples were stored for 24 h at room temperature over a desiccant so that the loosely bound water was removed. The specimens were weighed again and the corresponding mass gains are termed dry mass gains. The quantity of corrosion product was determined by leaching and pickling processes of the corroded specimens using agitating ultrasonic bath at room temperature, more details regarding the leaching and pickling are provided in [8].

The morphology of the corrosion products was examined by an FEI Quanta 200 environmental scanning electron microscopy (ESEM) with a Schottky field emission gun (FEG) both in the plane view and ion milled cross section investigations (see below). The instrument was equipped with Oxford Inca EDX system. The investigations were carried out in low vacuum with no need to cover the sample with a conductive layer. In order to perform imaging and EDX analyses different voltages were applied from 20 to 10 kV. 3D images of the specimen surface were obtained by atomic force microscopy (AFM, Q-Scope 350 from Quesant Instrument Corporation) in tapping mode (vibration frequency of 174 kHz) and analyzed using the Q-analysis 4.0 software package. The experiment was performed in air, at room temperature using an Agilent 5100 microscope (Agilent Technologies). Topographic AFM images of the surface were acquired (mapping of the relief of the surface in *x*, *y* and *z* directions).

TOF-SIMS analysis was performed using a ToF-SIMS V instrument (ION-ToF, GmbH, Münster, Germany) equipped with a 25 keV Bismuth LMIG (Liquid metal ion gun) and an 10 keV Cs sputter gun providing high precision information on the concentration of elements as a function of depth, at the Infrastructure for Chemical imaging at Chalmers University of Technology. Depth profiling and imaging was performed in the non-interlaced mode with 1 frame of analysis, 1 s of sputtering and 0.5 s pausing per cycle while using the floodgun for charge compensation. The Bi-LMIG was set in the high current bunched mode (mass resolution $m/\Delta m$: 6000; focus of the ion beam: 1–2 μm) using Bi_1 ions with a target current of 1 pA while Cs ions at 3 keV and 0.3 nA were used for sputtering. Both image and depth profile analyses were performed using the ION-ToF Surface Lab software (Version 6.3, ION-ToF, GmbH, Münster, Germany). The total primary ion flux was kept below 10^{12} ions/cm^2 to ensure static conditions for the surface imaging experiments. The distribution of elements after exposures was also studied on the cross sections of samples prepared by focused ion beam milling (FIB) methods using an FEI Versa 3D system. The FEI instrument used is equipped with both an electron and ion column. Thus, the FIB was able to image the specimen before, after, and during the milling by secondary electrons (SEs) or ions, which provides appropriate process control. Before milling, a layer of Ni was deposited on the corroded samples using physical vapor deposition (PVD) for protection of the surface.

3. Results

3.1. *Corrosion* versus *temperature*

The effect of temperature and NaCl on the rate of atmospheric corrosion of alloy AM50 is illustrated by Fig. 1, showing the dry mass gain and metal loss of samples after 672 h in 95% RH at two different levels of added NaCl. As expected, NaCl was quite corrosive toward alloy AM 50 while the rate of corrosion was low in the absence of salt (corresponding to <1 μm/year). In the presence of NaCl, there was a strong positive correlation between the rate of corrosion and temperature, the mass gains at 22 °C being approximately 9 times higher than at −4 °C at both levels of added salt. The effect of exposure temperature is apparent in Fig. 2, showing low magnification plan view images of the corroded surface after 672 h at −4 and 22 °C (70 μg/cm^2 NaCl). After exposure at −4 °C, SEM images revealed corrosion product accumulations with roughly circular shape on an otherwise smooth surface. The features correspond to NaCl (aq) droplets that formed when the samples were introduced into the 95% RH exposure environment. At 22 °C, most of the surface was covered by a thick layer of corrosion products, see Fig. 2b.

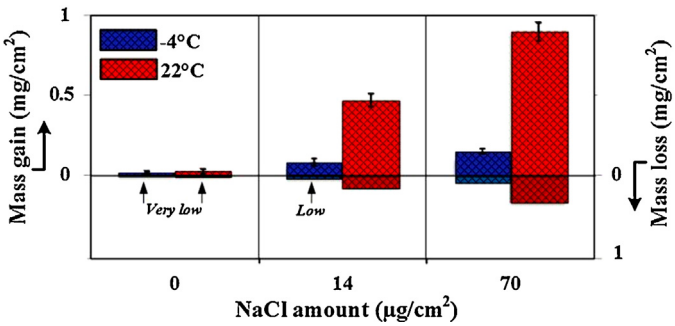

Fig. 1. The effect of temperature on the mass gain and metal loss of alloy AM50 (0, 14 and 70 μgcm^2, NaCl, 95% RH, 672 h).

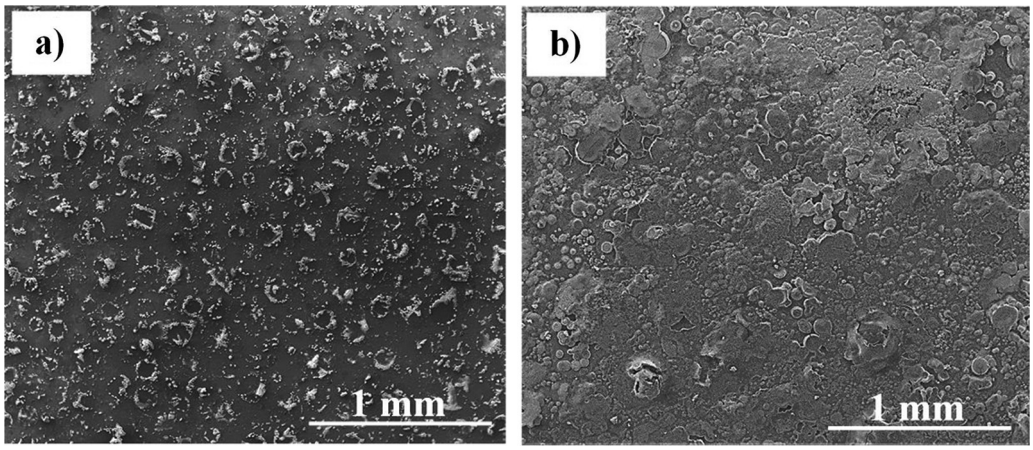

Fig. 2. SE-SEM images of alloy AM50 after 672 h exposure at 95%RH (70 μg/cm^2 NaCl) (a) −4 °C, (b) 22 °C. Note: The SEM micrograph of the samples exposed at 22 °C was captured from a heavily corroded region.

3.2. AFM mapping (localized corrosion at the early stages)

Fig. 2 shows corrosion product aggregates in the approximate size range 5–400 μm. The 3D rendered AFM images in Fig. 3 (24 h, 22 °C, 70 μg/cm^2 NaCl) provide topographic information at much higher resolution allowing features in the range 0.01–2 μm to be detected. Fig. 3b shows the localized nature of corrosion using color to highlight height differences. The image shows corrosion product agglomerations (red), surrounded by relatively flat regions (blue) showing little evidence for corrosion. In the following, the corroded surfaces are investigated by a combination of ToF-SIMS and SEM/EDX.

3.3. SEM/EDX analyses

The microscopy of corrosion was investigated by plan-view and cross-section SEM/EDX. Fig. 4 shows a SEM/EDX analysis of the sample in Fig. 2b (672 h, 22 °C, 70 μg/cm^2 NaCl). The corrosion product agglomerates were seen to be poor in Na^+ (P3, P5 in Fig. 4) while the relatively uncorroded areas between the crusts were sodium enriched (*e.g.* P1, P2 in Fig. 4). Also, the EDX analysis showed that the corrosion product crusts contained very little aluminum while the area between the large crusts exhibited a relatively strong Al signal. P1, representing the relatively uncorroded metal surface at a distance from the corrosion product crust, was very low in chlorine and high in sodium, suggesting a cathodic area. The presence of carbon at P1 is attributed to sodium carbonate formed by neutralization of the catholyte by CO_2. While P2 and P4 were closer to the corrosion product crust than P1, they were also high in Na and are interpreted as cathodic sites. The relatively weak O signal in P2 and P4 implied that a lot of the signal came from the alloy substrate. Hence, it is suggested that the relatively high Al signal in both P2 and P4 is due to the presence of β-phase particles and/or inter-dendritic regions in the alloy substrate. The small oxygen signal in P4 indicates that the corrosion product is relatively thin.

P3 and P5 represent the upper part of corrosion product crusts and were very low in Na and Al. In P3, the C/O and Mg/O ratio is 0.3 and 0.26. The corresponding ratios for $Mg_5(CO_3)_4(OH)_2 \times 4H_2O$ (hydromagnesite) are 0.22 and 0.27. The slightly higher C content detected by EDX was likely related to contamination during sample handling. Thus, these corrosion crusts were interpreted as mainly consisting of Mg hydroxy carbonates. This is in line with lab [11,12] and field exposures [13–15] in the literature that report on the formation of several Mg hydroxy carbonates, including hydromagnesite, during atmospheric corrosion of Mg alloys in the presence of NaCl. The small amount of Si detected in P2 was likely introduced during sample preparation.

Fig. 5 shows SEM/FIB/EDX analyses of the sample in Fig. 2a (672 h, −4 °C, 70 μg/cm^2 NaCl). The plan-view SEM image in Fig. 5a shows a typical corrosion morphology developed at −4 °C. The boxed area shows where the FIB cross section was prepared. The EDX chlorine map in Fig. 5c shows that Cl is enriched in the corrosion pits. Similarly, cross section EDX analysis of samples subjected to a corresponding exposure at 22 °C (not shown), also indicated that Cl was concentrated in the corrosion pits.

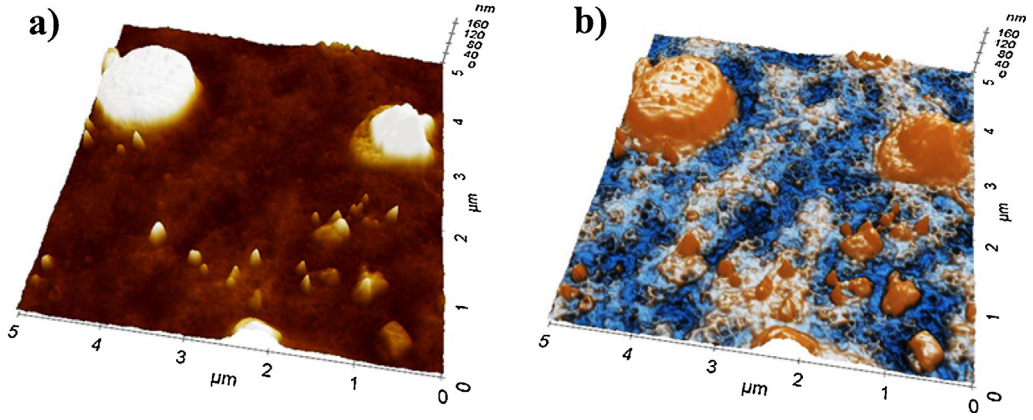

Fig. 3. (a) 3D rendered AFM image after 24 h exposure at 22 °C, 70 μg/cm^2 NaCl, (b) the corresponding enhanced-color-contrast 3D-rendered AFM image.

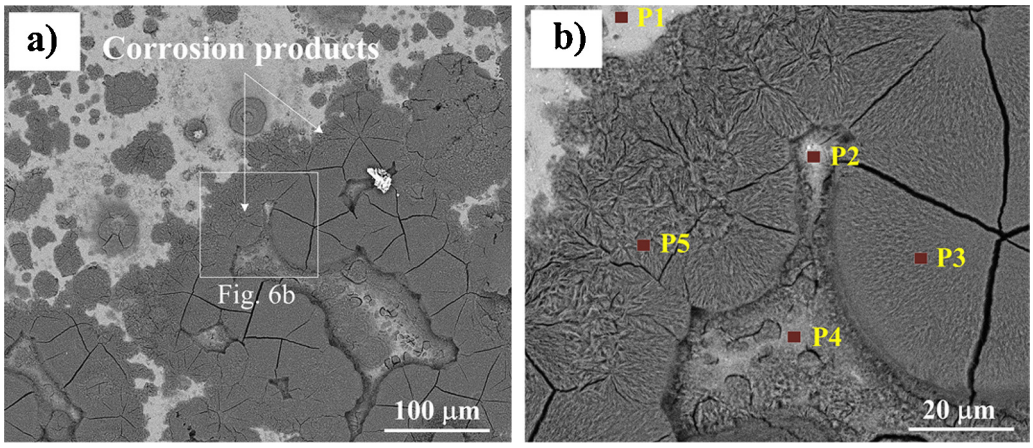

Fig. 4. (a) Low magnification plan view SEM image of the corroded surface (70 μg/cm^2 NaCl, 672 h, 22 °C). (b) A close-up SEM image showing the boxed region in (a). Note: the EDX point analysis of P1, . . ., P5 are presented in Table 2.

3.4. ToF-SIMS surface analyses

Fig. 6 shows a ToF-SIMS analysis of the corroded surface after 672 h at 22 °C (70 μg/cm^2 NaCl) (compare Figs. 2b and 6). The images were acquired using positive polarity and include maps for the different cations and the total ion image. Ion imaging is affected by topography in several ways. Firstly, the primary ions do not reach areas shadowed by the corrosion product accumulations (up to 160 nm high in this case) and these areas (on the edge of the corrosion product accumulations) also do not emit secondary ions. Shadowed areas appear black in the ToF-SIMS total ion signal, see Fig. 6j, and contribute little or no information on surface chemistry. Secondly, high areas on the surface are subjected to a greater extraction field in the ToF-SIMS analysis and hence give rise to a stronger ion signal than low areas. This tends to obscure the compositional gradients on the surface that we wish to study. Also, a rough topography causes a decrease in mass resolution since ions with the same mass and charge will arrive at the detector at different times depending on whether it travels from a high or low area.

To circumvent the problems related to surface topography, and enable the extraction of chemical information from the rough surface by ToF-SIMS, Figs. 6a–i shows both the full ToF-SIMS maps and SIMS maps of high and low areas separately. As expected, the "full" Mg map shows a relatively even Mg^+ signal, of course, excluding the "shadowed" regions (compare Fig. 6j). The sodium distribution observed by ToF-SIMS is affected by artifacts caused by Na^+ migration in the electric field [16]. Anyway, Figs. 6d–f shows that the Na^+ signal tends to be stronger in the low areas than in the high areas. This implies that Na^+ is accumulated in the relatively uncorroded areas between the corrosion product aggregates. The Al^+ signal (Figs. 6g–i) is very weak making it difficult to observe the Al^+ distribution on the surface.

Fig. 7 shows the results of a high-magnification ToF-SIMS analysis with negative polarity performed after an exposure identical to that illustrated in Fig. 6, presenting ion images for Cl^-, AlO^- and $MgOH^-$. It may be noted that positive and negative ion images cannot be acquired from the same area. The area analyzed in Fig. 7 is in the middle of a large α-Mg grain which was partly covered by corrosion product crusts. Prior to the ToF-SIMS analysis the area was examined by SEM/EDX. The approximate location of the crusts is indicated by the dashed circles in the AlO^- map. Chloride is present in the corrosion crusts while it is absent from the other regions. In contrast, AlO^- and $MgOH^-$ are detected on the parts of the surface not covered by corrosion product crusts. As noted above, the areas not covered by corrosion product accumulations are also enriched in Na^+ (compare Fig. 6e and f).

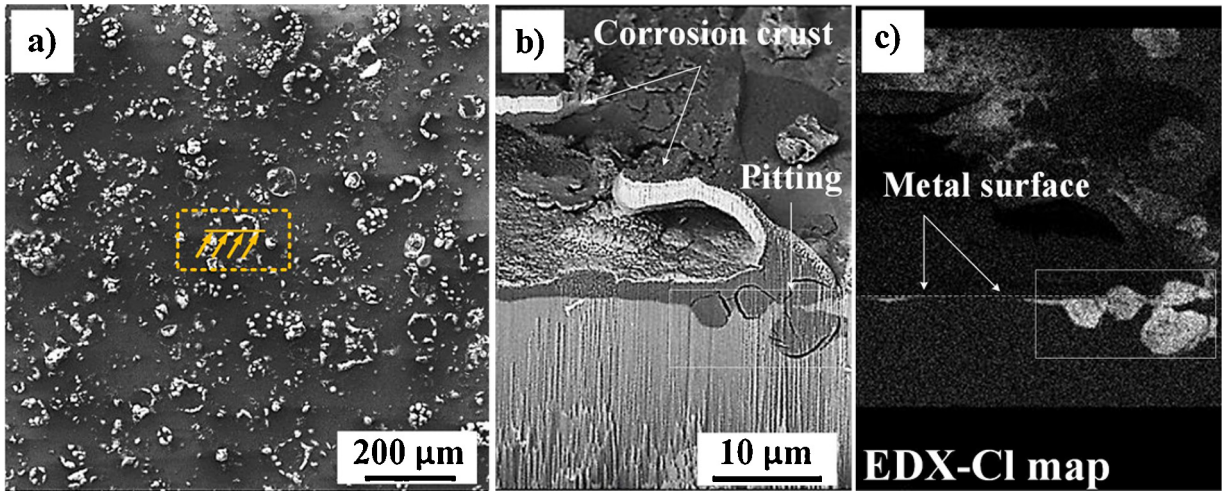

Fig. 5. (a) Top-view SEM-BSE micrograph of HPDC AM50 after 672 h at −4 °C (14 μg/cm^2 NaCl), (b) a FIB-prepared cross section at the site indicated in (a), and (c) the corresponding EDX chlorine map.

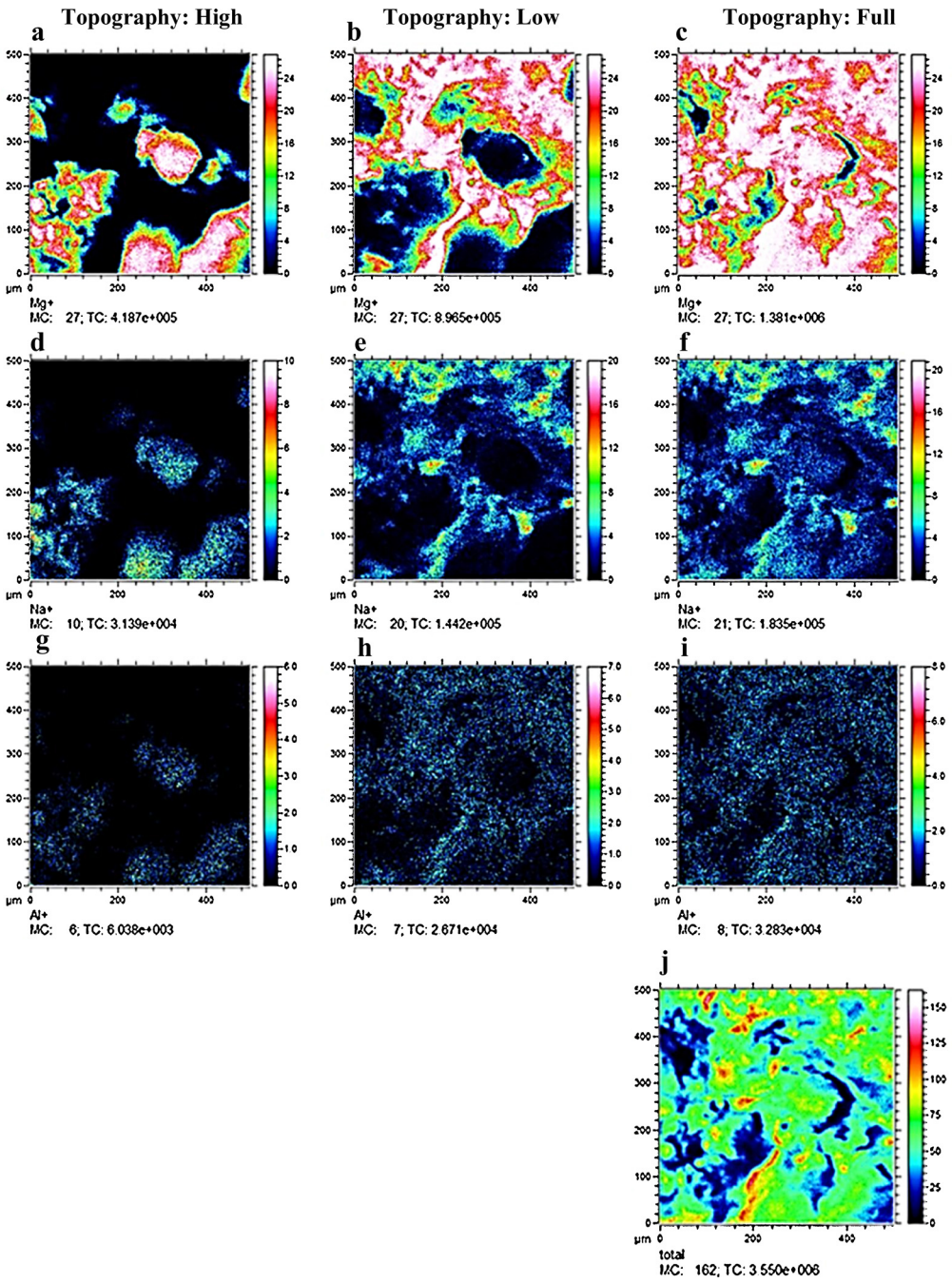

Fig. 6. ToF-SIMS surface analysis of alloy AM50 after 672 h at 22 °C (70 μg/cm^2 NaCl) showing the effect of topography on different ion signals; (a, b and c) Mg^+, (d, e and f) Na^+, (g, h and k) Al^+. The left column shows signals from high areas (approx. 160 nm above the alloy surface), the middle column shows the signal from low areas (corresponding to the surface of the uncorroded alloy). The column to the right shows signals from the full topography range, and (j) the ToF-SIMS total ion signal (all cations).

3.5. *ToF-SIMS depth profiling*

ToF-SIMS depth profile analyses with positive ion charge were conducted on samples exposed at −4 and 22 °C respectively, (672 h, 70 μg/cm^2 NaCl). Two representative profiles are shown in Fig. 8. The analyses were performed on relatively small (<50 μm) isolated corrosion crusts situated in the middle of α-Mg grains. The ToF-SIMS depth profiling analysis includes the entire corrosion product crust while the uncorroded neighboring parts of the α−Mg substrate are excluded. Hence, the depth profile provides a 3d topographical image of the corrosion product crust and of the corresponding corrosion pit. Thus, the lower boundary of the cation distribution maps corresponds to the corroded metal surface, showing several corrosion pits. Mn and Zn were below the detection limit of the survey scans. Small amounts of Al^+ were detected (shown in the graphs). Si^+ was detected occasionally, appearing as small particles in the SIMS maps (see the 3D images in Fig. 8). The analysis starts at the surface and then successively probes deeper into the corrosion product crust/corrosion pit. Na^+, Mg^+, Al^+ and Si^+ are rendered in Fig. 8, visualizing the distribution in 3D. The shape of the pits is visualized in the "total" (=all cations) maps in Fig. 8. Measurements performed on several crusts revealed that the ion yields were independent of crust size. In contrast, the ion yields depended strongly on exposure temperature. Comparing the results obtained at the two temperatures, the most noticeable difference is in the intensity and distribution of Na^+ and Mg^+. It is

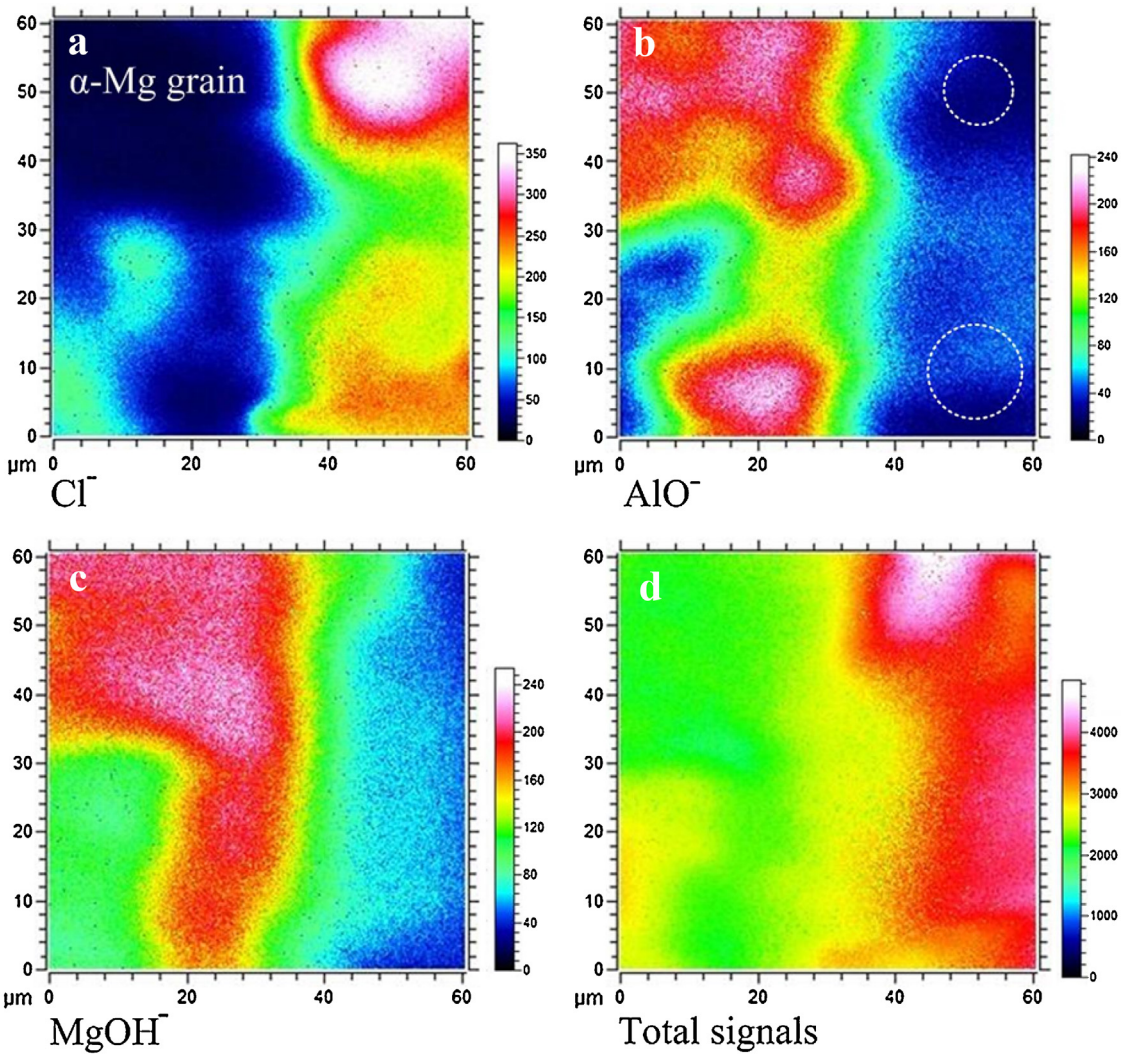

Fig. 7. ToF-SIMS analysis of alloy AM50 after 672 h at 22 °C (70 μg/cm² NaCl); (a) Cl^- ions, (b) AlO^- ions, (c) $MgOH^-$ ions, (d) the corresponding ToF-SIMS total signals map (all anions). The dashed circles in the AlO^- map corresponds to the location of corrosion product crusts.

cautioned that ToF SIMS does not provide quantitative information on the amounts of Na^+ and Mg^+. However, the profiles in Fig. 8 do show that the Na+/Mg+ ratio is 'much higher at −4 °C than at 22 °C. Ion intensity data from the depth profiles acquired with the same ion dose indicated a Na^+/Mg^+ signal ratio of 3.9 on samples exposed at −4 °C and of 0.4 at 22 °C. A semi-quantitative analysis of the Na^+ ion intensity normalized to the primary ion dose density revealed that the Na^+ level after exposure at −4 °C was approximately 20 times higher than at 22 °C. A ToF-SIMS depth profile analysis with negative polarity was obtained from corrosion crusts formed on the samples exposed at −4 and 22 °C (see Fig. 9). In this case, the corrosion crusts were removed mechanically before depth profiling. Hence, the analysis probes the corrosion product in the pits. The profile shows that Cl^- is indeed present in the pits, in accordance with the FIB/EDX analysis in Fig. 5c. It may be noted that the intensity of the chloride signal was higher in the corrosion pits formed at 22 °C than −4 °C.

4. Discussion

4.1. Electrochemical nature of the corrosion process

The localized nature of the atmospheric corrosion of alloy AM50 in the presence of NaCl is clearly demonstrated by the present study. It is illustrated by the AFM imaging (Fig. 3), by the plan view SEM images in Figs. 4 and 5a, the cross section SEM/EDX analysis (Fig. 5b and c) as well as by the ToF-SIMS (Fig. 7) analysis of a corrosion product crust and the underlying corrosion pit. This is in accordance with several reports on the corrosion behavior of Mg and Mg alloys in the literature [17–20].

The corrosion of Mg and Mg alloys in the presence of alkali salt solutions is usually described in terms of an electrochemical corrosion process involving the cathodic evolution of hydrogen and the anodic dissolution of Mg [17]. The corrosion cells give rise to concentration gradients, including pH gradients, between anodic and cathodic areas on the metal surface. Because of the small amount of surface electrolyte available under atmospheric corrosion conditions and the lack of convection in the electrolyte, the corrosion experiments in the present study are expected to generate strong concentration gradients.

Accordingly, subjecting alloy AM50 to corrosion at 22 °C resulted in a redistribution of Na^+ and Cl^- on the corroded surface, as illustrated by the Fig. 4 and by the EDX point analysis in Table 2. Thus, high concentrations of sodium were detected on the relatively uncorroded alloy surface while chlorine was detected in the corrosion product crusts. The observed chemical gradients thus support a scenario where electrochemical corrosion cells are active.

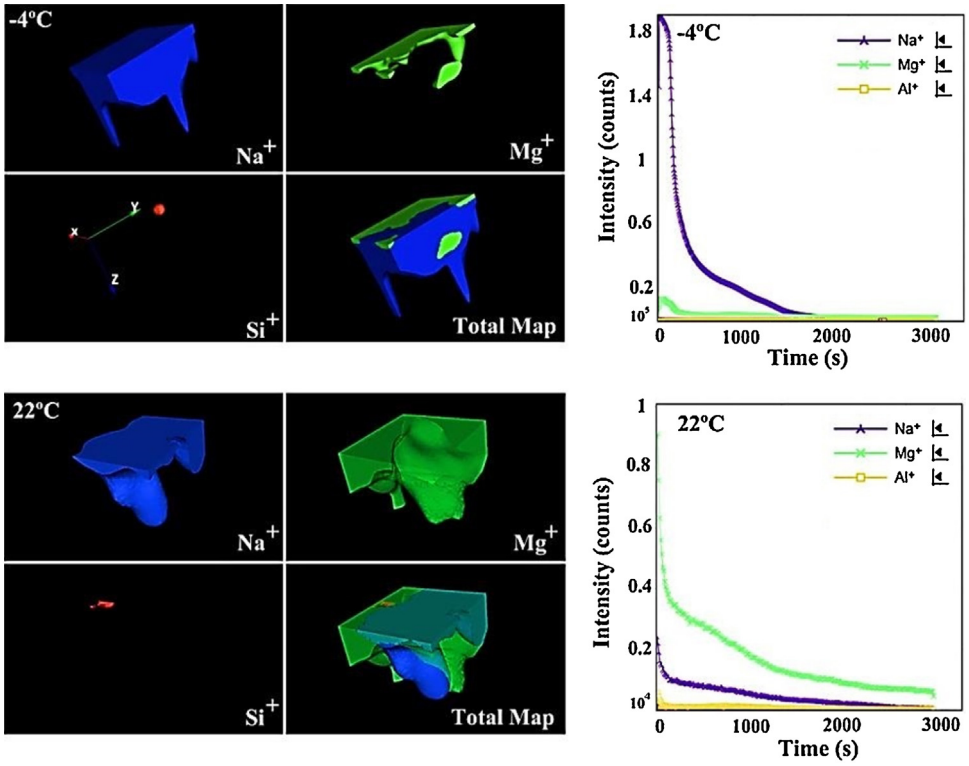

Fig. 8. The ToF-SIMS depth profiling maps (positive polarity) after exposure at −4 and 22 °C.

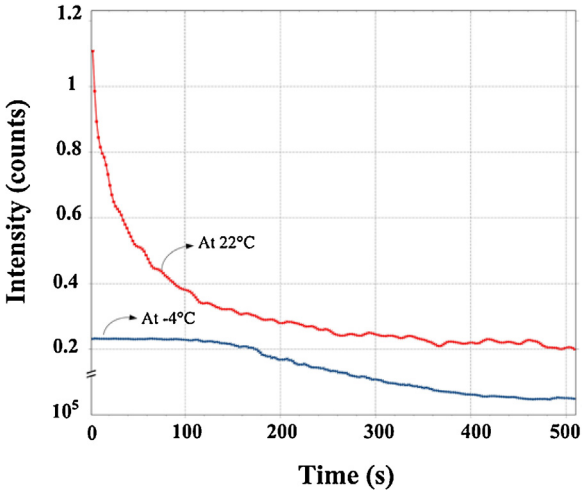

Fig. 9. ToF-SIMS depth profiling with negative polarity showing the Cl^- signal as a function of sputtering time after 672 h exposure at −4 and 22 °C.

4.2. Temperature dependence of corrosion

Fig. 5 shows that corrosion was localized also at −4 °C even though the rate of corrosion was much slower at −4 °C than at 22 °C, (see Figs. 1, 2 and 6). Also, EDX analysis of the cross section (Fig. 5c) shows that chloride is enriched in the corrosion pits, similar to the situation at 22 °C. This may indicate electrochemical corrosion process is also active at −4 °C. However it is cautioned that other corrosion mechanism(s) may also be active at sub-zero temperature, see below. In the experimental conditions (95% RH, −4, 22 °C) NaCl absorbs water to form an aqueous solution on the metal surface. Also, the equilibrium composition of the resulting solution is reported to be nearly the same at the two temperatures (=8.0% NaCl by weight) [21]. This implies that the effect of temperature on corrosion behavior is not due to differences in the availability of water on the surface or to electrolyte concentration. Previously, it was shown that CO_2 inhibits the atmospheric corrosion of both Mg and Mg alloys and Al in the presence of NaCl [12,22]. The effect was explained by the neutralization of the catholyte by CO_2 which tends to decrease surface conductivity and causes precipitation of slightly soluble Mg hydroxy carbonates. Thus, it could be argued that the observed temperature effect may be connected to the corrosion inhibiting effect of CO_2, *e.g.*, to the increasing solubility of CO_2 in the surface electrolyte with decreasing temperature. Also, the absence of a significant temperature effect for the corrosion of pure Mg [8] implies that the observed temperature effect cannot be explained by the temperature dependence of the conductivity of the surface electrolyte.

The strong acceleration of atmospheric corrosion with increasing temperature for alloy AM50 (see Fig. 1) in the presence of NaCl

Table 2
EDX analyses (at.%) of the 5 positions shown in Fig. 4b.

Analyzed points	Mg	O	Na	C	Al	Cl	Si
P1	25.5 ± 0.2	29.8 ± 0.1	30.6 ± 1.3	6.4 ± 0.1	7.4 ± 0.2	0.3 ± 0.1	–
P2	30 ± 0.1	23 ± 0.4	19 ± 0.2	5 ± 0.4	20 ± 1	2.4 ± 0.1	0.6 ± 0.1
P3	16 ± 0.5	59.5 ± 0.7	0.5 ± 0.4	18.6 ± 1.9	–	5.4 ± 0.1	–
P4	31 ± 1.1	11 ± 0.3	25 ± 1.7	8.5 ± 0.3	20 ± 2.6	4.5 ± 0.3	–
P5	15 ± 0.3	57.2 ± 0.1	0.9 ± 0.2	26 ± 2.1	–	0.9 ± 0.1	–

is in line with a recent paper by this group [8]. In contrast, the rate of corrosion of commercially pure Mg was reportedly not accelerated by increasing temperature. Similar to the present results, Blücher et al. [22] reported a strong positive correlation between temperature and corrosion rate for the atmospheric corrosion of aluminum in the presence of NaCl in the range 4–60 °C. This suggests that the strong positive correlation between exposure temperature and corrosion rate observed for alloy AM50 is connected to the aluminum content. Thus, it has been suggested that the strong correlation of the rate of Mg corrosion with temperature is due to an activated process involving aluminum, possibly the dissolution of alumina present in the passive film [8].

4.3. ToF SIMS surface analysis

In comparison to the tool-box of modern microscopy, including EDX analysis of FIB milled cross sections, SIMS offers a greater surface sensitivity and the possibility to prepare profiles through the corroded surface. Also, the inherent high sensitivity for alkali and halide ions implies that ToF-SIMS analysis can help elucidate corrosion processes where halide salts play a role. The results from the ToF-SIMS surface analysis after exposure at 22 °C were broadly in line with the SEM/EDX analysis. Thus, ToF-SIMS showed that sodium tends to be concentrated in the low areas, corresponding to the relatively uncorroded alloy surface (Fig. 6), while Cl^- was associated with the corrosion product aggregates (Fig. 7). This supports the electrochemical cell scenario with anodic regions suffering pitting and cathodic regions where the alloy is protected from corrosion due to high pH.

The distribution of Cl^- ions on the corroding surface is important because Cl^- has been shown to become incorporated into the film structure, and consequently accelerate the breakdown of the quasi-passive film formed on Mg and Mg alloys [23–26]. The present study (see Fig. 7) shows that the distribution of Cl^- on the corroded surface can be investigated by ToF-SIMS surface analysis with negative polarity. However, lack of quantitative information limits the usefulness of ToF SIMS in this respect.

It is interesting to compare the positive and negative polarity maps, *i.e.* the ionic distribution of Al^+ *versus* AlO^- and Mg^+ *versus* $MgOH^-$ in Figs. 6 and 7. For example, the distribution of Mg^+ is different from that of $MgOH^-$ (compare Figs. 6 and 7). Thus, while Mg^+ cations were detected both on the corrosion product aggregates and on the unreacted regions, $MgOH^-$ was mainly detected in the unreacted areas. Also, a comparison of the Al^+ and AlO^-, maps shows interesting differences. Thus, while Fig. 7g shows that Al^+ is present everywhere on the surface although at very low intensity, $AlOH^-$ appears only in the low (uncorroded) regions of the α-Mg grain and not in the corroded regions. The emission of Al^+ cations from the corrosion product aggregates appears to contradict the EDX point analysis which showed that corrosion products do not contain Al. The conflicting evidence may be due to artifacts in the ToF-SIMS analysis or to the detection limit of the EDX.

It is suggested that the distribution of positive and negative Mg- and Al-containing ions in the ToF-SIMS analysis contains information on the surface chemistry. Thus, it is suggested that the negative ions ($MgOH^-$ and AlO^-) are generated from high pH areas while the positive Al and Mg ions emanate from areas with lower pH. Also, it is suggested that the $MgOH^-$ and AlO^- and ions emitted from the uncorroded regions originate from the surface film. The films formed on Mg and Mg alloys have been mainly analyzed using transmission electron microscopy (TEM), TEM/EDX and AES, see for *e.g.* [4,6,26–30]. Seyeux et al. [7], who used ToF-SIMS for analyzing the surface films formed on pure Mg, reported that the film, formed during dry-polishing, after aging in H_2O at the corrosion potential (E_{corr}) for 120 s was a mixture included of $Mg(OH)_2$, in the outer layer, MgO, in the inner layer, and traces of MgH_2. Taheri et al. [26] who studied the film formed on pure Mg corroding in 0.01 M NaCl reported that it was comprised mainly of a Mg oxide (MgO) region adjacent to the Mg-film interface and a more porous mixed MgO and $Mg(OH)_2$ region adjacent to the film/electrolyte interface. Using TEM/EDX, Brady et al. [4] reported that the surface layer formed on Mg alloys in water contained $Mg(OH)_2$, hydrated MgO and an alumina-rich component.

It is considered that the presence of alumina will fundamentally influence film properties. While $Mg(OH)_2$ is insoluble in strongly alkaline conditions and forms stable passive films in the cathodic areas, it is soluble in neutral solutions, facilitating the anodic dissolution of magnesium. In contrast, alumina ($Al(OH)_3$) is soluble at high pH, forming aluminate ($Al(OH)_4^-$) ions and is insoluble in neutral solution. Hence, the presence of an alumina component in the passive film is expected to inhibit the anodic dissolution of the alloy. Also, it is suggested that the tendency for the corrosion properties of Mg alloys to improve with increasing Al content can be attributed to the presence of alumina in the surface film. The corrosion properties of aluminum in aqueous solution have been widely investigated and the accelerating role of chloride ions is well documented [31–34]. Thus, it has been shown that the formation of Al-Cl bonds at the film surface weakens the Al—O bonds in the passive film, facilitating its dissolution [34–36]. Altogether, the present results suggest that ToF-SIMS surface analysis is a useful tool for analyzing the passive films on Mg alloys. For instance, one could study/compare the intensities of the AlO^- ions acquired from the top of various microstructural constituents in Mg alloys using normalized ToF-SIMS data. This will provide information regarding the ability of Mg alloys in developing alumina-containing passive layers on their surfaces.

4.4. ToF-SIMS depth profiling

The ToF-SIMS depth profiling after exposure at −4 and 22 °C, provides a detailed view of corrosion pits and the overlying corrosion product accumulation. In contrast to the SEM/EDX analysis on the corroded surfaces (see Fig. 4 and Table 2), the cation analysis in Fig. 8 reveals that both Na^+ and Mg^+ are present in the corrosion product crust and in the underlying corrosion pit. The corresponding anionic depth profile in Fig. 9 shows that chloride is indeed present in the corrosion pit at the both temperatures. The accumulation of chloride in the corrosion pits is in accordance with the EDX results (Fig. 5) and with a recent study [37], where Mg alloys were subjected to salt-spray and immersion exposures. In contrast, there is reportedly little evidence for chloride in the corrosion pits on field exposed Mg alloys (see for *e.g.* [15]). The lack of evidence for chloride in the corrosion pits in the outdoor environment is tentatively attributed to a relatively low exposure to chloride in combination with leaching by rain. It may be noted that the use of de-icing salt on the roads creates a corrosive environment in the wintertime which is far richer in chloride than typical urban or industrial atmospheric corrosion test sites. In the present work, the availability of chloride is high and there is no leaching by rain.

The ToF-SIMS depth profile analysis shows that the concentration of Cl^- ions in the anodic sites strongly depended on exposure temperature. As seen in Fig. 10, the amount of Cl^- ions is much higher in the pit formed at 22 °C than −4 °C. This indicates that there is little migration of Cl^- at −4 °C implying that electrochemical corrosion cells are more active at the higher temperature. Similar to chloride, the depth profile cation analysis in Fig. 9 shows that the Na^+ ion intensity is different for samples exposed at −4 and 22 °C. Thus, the Na^+ intensity was relatively high in the vicinity of the corrosion crusts after exposure at −4 °C, which was not the case for the sample exposed at 22 °C. Similarly high Na^+ intensities were observed in the corrosion pits on several other samples exposed at −4 °C. At 22 °C sodium was mainly detected at a distance from

the corrosion products (Fig. 7 and P2 and P4 in Table 2). The very high intensity of Na^+ ions around corrosion crusts at −4 °C implies that there is little migration of Na^+, while Na^+ migrates significantly toward cathodic sites at 22 °C.

At 22 °C the chemistry of the pit, being high in chloride and low in sodium, is in accordance with electrochemical corrosion cell where the pit acts as the anode. In contrast, the relatively low accumulation of chloride and high concentration of in the pits after exposure at −4 °C suggests that electrochemical corrosion is less prominent. Hence it is hypothesized that the corrosion of alloy AM 50 at −4 °C largely do not involve macroscopic electrochemical cells and that both magnesium oxidation and hydrogen evolution occur simultaneously within the pit. Thus, a hypothesis would be the occurrence of a "chemical corrosion" at sub-zero-temperatures, meaning that the reaction of water with Mg occurs locally ($Mg(s) + H_2O \rightarrow MgO(s) + 2H$), only involving the transfer of charge between individual atoms and molecules and generating no measurable electronic current. Future work is planned in order to investigate the corrosion mechanisms and the composition of corrosion products formed at sub-zero temperature using ToF-SIMS analyses in combination with other analytical techniques such as TEM and AES.

5. Conclusion

The redistribution of ionic species in the atmospheric corrosion of the alloy AM50 is investigated by ToF-SIMS analysis and the results were compared to EDX analyses on the plan-view SEM and FIB-prepared cross sections. The ToF-SIMS contaminant distribution imaging showed high localized concentrations of ionic species in and around the cathodic and anodic sites. It is observed that sodium ions and/or sodium rich compounds are mainly accumulated in a distance from the anodic sites. The chlorine ions, however, are present in the anodic sites and also in the corrosion pits indicating an active corrosion process in the case of the samples exposed at 22 °C. In the case of the samples exposed at −4 °C, however, the sodium ions were not migrated toward the cathodic sites, suggesting the influence of temperature on the conductivity of the thin electrolyte layer formed on the metal surface. Besides, the concentration of chlorine ions was much less in the corrosion pits formed at −4 °C. The results clearly confirm the less active corrosion process at sub-zero temperature. Interestingly, ToF-SIMS showed a promising capability to study the thin passive films containing AlO^- and $MgOH^-$ on the surface of the corroded Mg alloys.

References

[1] M. Collinet-Fressancourt, N. Nuns, S. Bellayerc, M. Traisnel, Appl. Surf. Sci. 277 (2013) 186–191.
[2] M. Kubicek, G. Holzlechner, A.K. Opitz, S. Larisegger, H. Hutter, J. Fleig, Appl. Surf. Sci. 289 (2014) 407–416.
[3] C.-C. Chang, C.-C. Wang, C.-W. Wu, S.-C. Liu, F.-D. Mai, Appl. Surf. Sci. 255 (2008) 1531–1533.
[4] M.P. Brady, M. Fayek, H.M. Meyer III, D.N. Leonard, H.H. Elsentriecy, K.A. Unocic, L.M. Anovitz, E. Cakmak, J.R. Keiser, G.L. Song, B. Davis, Scrip. Mater. 106 (2015) 38–41.
[5] A. Seyeux, M. Liu, P. Schmutz, G. Song, A. Atrens, P. Marcus, Corros. Sci. 51 (2009) 1883–1886.
[6] K.A. Unocic, H.H. Elsentriecy, M.P. Brady, H.M. Meyer III, G.L. Song, M. Fayek, R.A. Meisner, B. Davis, J. Electrochem. Soc. 161 (2014) C302–C311.
[7] A. Seyeux, G.S. Frankel, N. Missert, K.A. Unocic, L.H. Klein, A. Galtayries, P. Marcus, J. Electrochem. Soc. 158 (2011) C165–C171.
[8] M. Esmaily, M. Shahabi-Navid, J.E. Svensson, M. Halvarsson, L. Nyborg, Y. Cao, L.G. Johansson, Corros. Sci. 90 (2015) 420–433.
[9] M. Esmaily, M. Shahabi-Navid, N. Mortazavi, J.E. Svensson, L.G. Johansson, Mater. Charac. 95 (2014) 50–64.
[10] M. Esmaily, N. Mortazavi, M. Shahabi-Navid, J.E. Svensson, M. Halvarsson, L. Nyborg, A.E.W. Jarfors, M. Wessén, L.G. Johansson, J. Electrochem. Soc. 162 (2015) C85–C95.
[11] M. Esmaily, M. Shahabi-Navid, N. Mortazavi, J.E. Svensson, M. Halvarsson, Y. Cao, L.G. Johansson, J. Electrochem. Soc. 162 (2015) C311–C321.
[12] M. Shahabi-Navid, M. Esmaily, J.E. Svensson, M. Halvarsson, L. Nyborg, Y. Cao, L.G. Johansson, J. Electrochem. Soc. 161 (2014) C277–C287.
[13] J. Liao, M. Hotta, Corros. Sci. 100 (2015) 353–364.
[14] M. Jönsson, D. Persson, C. Leygraf, Corros. Sci. 50 (2008) 1406–1413.
[15] J. Liao, M. Hotta, S. Motoda, T. Shinohara, Corros. Sci. 71 (2013) 53–61.
[16] J. Grams, New Trends and Potentialities of ToF-SIMS in Surface Studies, Nova Science Publisher, 2007.
[17] S. Thomas, N.V. Medhekar, G.S. Frankel, N. Birbilis, Curr. Opin. Solid State Mater. Sci. 19 (2015) 85–94.
[18] C. Liu, J. Liang, J. Zhou, L. Wang, Q. Li, Appl. Surf. Sci. 343 (2015) 133–140.
[19] S. Feliu Jr., A. Pardo, M.C. Merino, A.E. Coy, F. Viejo, R. Arrabal, Appl. Surf. Sci. 255 (2009) 4102–4108.
[20] M. Esmaily, N. Mortazavi, J.E. Svensson, M. Halvarsson, L.G. Johansson, Ultramicroscopy 153 (2015) 45–54.
[21] R.J. Bodnar, Geochim. Cosmochim. Acta 57 (1993) 683–684.
[22] D.B. Blücher, J.E. Svensson, L.G. Johansson, J. Electrochem. Soc. 150 (2013) B93–B98.
[23] M.C. Merino, A. Pardo, R. Arrabal, S. Merino, P. Casajús, M. Mohedano, Corros. Sci. 52 (2010) 1696–1704.
[24] .R. Kish, Y. Hu, J. Li, W. Zheng, J.R. McDermid, Corrosion 68 (2012) 468–474.
[25] A. Pardo, M.C. Merino, A.E. Coy, R. Arrabal, F. Viejo, E. Matykina, Corros. Sci. 50 (2008) 823–834.
[26] M. Taheri, M. Danaie, J.R. Kish, J. Electrochem. Soc. 161 (2014) C89–C94.
[27] R.C. Phillips, J.R. Kish, Corrosion 69 (2013) 813–820.
[28] M. Taheri, J.R. Kish, J. Electrochem. Soc. 160 (2013) C36–C41.
[29] M. Danaie, R.M. Asmussen, P. Jakupi, D.W. Shoesmith, G.A. Botton, Corros. Sci. 77 (2013) 151–163.
[30] M.P. Brady, G. Rother, L.M. Anovitz, K.C. Littrell, K.A. Unocic, H.H. Elsentriecy, G.L. Song, J.K. Thomson, N.C. Gallego, B. Davis, J. Electrochem. Soc. 162 (2015) C140–C149.
[31] G.S. Frankel, J. Electrochem. Soc. 145 (1998) 2186–2198.
[32] Z. Szklarska-Smialowska, Corros. Sci. 41 (1999) 1743–1767.
[33] J. Kruger, Int. Mater. Rev. 33 (1988) 113–130.
[34] H.H. Strehblow, Mechanisms of Pitting Corrosion in Corrosion Mechanisms in Theory and Practice, Marcel Dekker, New York, Basel, 2002.
[35] P.M. Natishan, E. McCafferty, G.K. Hubler, J. Electrochem. Soc. 133 (1986) 1061–1062.
[36] P.M. Natishan, W.E. O'Grady, J. Electrochem. Soc. 161 (2014) C421–C432.
[37] W. Song, H.J. Martin, A. Hicks, D. Seely, C.A. Walton, W.B. Lawrimore, P.T. Wang, M.F. Horstemeyer, Corros. Sci. 78 (2014) 353–368.